Strain localization and the onset of dynamic weakening in fault gouge

S.A.F. Smith[1], S. Nielsen[2] & G. Di Toro[3,4]

[1]Department of Geology, University of Otago, Dunedin 9054, New Zealand

[2]Rock Mechanics Laboratory, Department of Earth Sciences, Durham University, Durham, England

[3]Istituto Nazionale di Geofisica e Vulcanologia (INGV), Rome 00143, Italy

[4]Dipartimento di Geoscienze, Università degli Studi di Padova, Via G. Gradenigo 6, 35131, Padova, Italy

Corresponding author e-mail: steven.smith@otago.ac.nz

Corresponding author telephone: +64 03 479 7515

Corresponding author fax: +64 03 479 7527

Abstract

To determine the role of strain localization during dynamic weakening of gouge at seismic slip rates, single-slide and slide-hold-slide experiments were conducted on 2-3-mm thick layers of calcite gouge at normal stresses up to 26 MPa and slip rates up to 1 m s^{-1}. Microstructures were analyzed from short displacement (<0.35 m) experiments stopped prior to and during the transition to dynamic weakening. In fresh calcite gouge layers, dynamic weakening occurs after a prolonged initial strengthening phase that becomes shorter with increasing normal stress and decreasing layer thickness. Strain is initially distributed across the full thickness of the gouge layer, but quickly becomes localized to a boundary-parallel, high-strain shear band c. 20 μm wide. During the initial strengthening phase the shear band broadens to become c. 100 μm wide at peak stress. The transition to dynamic weakening in calcite gouges is associated with a change from layer dilation to compaction and the appearance of many short and isolated slip surfaces within the shear band. Each individual slip surface is surrounded by aggregates of extremely fine grained and tightly packed calcite, interpreted to result from grain welding driven by local frictional heating in the shear band. By the end of dynamic weakening, deformation is extremely well localized to a single 2-3-μm wide principal slip surface, flanked by layers of recrystallized gouge. Calcite gouge layers re-sheared following a hold period behave mechanically like solid cylinders of calcite marble, due to reactivation of the principal slip surface formed during the first slide reducing the effective gouge layer thickness to a few microns. Our results suggest that formation of a high-strain shear band is a critical precursor to dynamic weakening in calcite gouges. Microstructures are most compatible with dynamic weakening in gouges resulting from a thermally triggered mechanism such as flash heating that requires both a high degree of strain localization and a minimum slip velocity to activate.

Keywords: Localization; Gouge; Dynamic Weakening; Microstructure; Earthquakes

Highlights:

- Experiments on calcite gouges to investigate strain localization and dynamic weakening
- Formation of high-strain shear band is critical precursor to dynamic weakening
- Dynamic weakening correlates with formation of short slip surfaces in shear band
- Observations compatible with gouge dynamic weakening by flash heating in shear band
- Re-sheared calcite gouge layers behave like solid marble

1. Introduction

Mid- to upper-crustal crustal fault zones contain layers of finely comminuted material known as fault gouge, formed by particle fracturing, surface wear and fluid-rock interactions (e.g. Ben-Zion and Sammis, 2003; Chester and Logan, 1987; Engelder, 1974; Scholz, 1987; Sibson, 1977). Field observations indicate that fault displacements are often focused in to narrow gouge-bearing fault cores (e.g. Ben-Zion and Sammis, 2003; Caine et al., 1996; Chester and Chester, 1998; Chester et al., 2004; Faulkner et al., 2010; Sagy and Brodsky, 2009; Schulz and Evans, 2000; Wibberley and Shimamoto, 2003). There is also increasing evidence to suggest that seismic slip during earthquakes occurs largely within gouge-bearing slip zones on the order of a few millimeters or less in thickness (e.g. Boullier et al., 2009; Chester and Chester, 1998; Collettini et al., 2013; De Paola et al., 2008; Fondriest et al., 2012; Heesakkers et al., 2011; Li et al., 2012; Mizoguchi et al., 2008; Otsuki et al., 2003; Sibson, 2003; Smith et al., 2011; Wibberley and Shimamoto, 2003).

Laboratory experiments have demonstrated that bare rock surfaces and gouge layers experience dynamic weakening when the slip velocity and sliding displacement approach values characteristic of earthquakes (Di Toro et al., 2011). A variety of physical mechanisms have been proposed to explain the dynamic weakening behavior observed in the laboratory and postulated to occur in natural faults. In particular, mechanical and microstructural data collected from experiments performed on solid rocks (bare surfaces) are consistent with the activity of flash heating and weakening at asperity contacts (Beeler et al., 2008; Goldsby and Tullis, 2011; Kohli et al., 2011; Rice, 2006), silica gel lubrication (Di Toro et al., 2004) and frictional melting (Di Toro et al., 2006; Nielsen et al., 2008).

Gouge layers deformed at high velocities typically show a narrow (<100 μm) and fine-grained shear localization zone cut by a discrete sliding surface or multiple surfaces coated with extremely small (“nano”) or sintered grains (e.g. Brantut et al., 2011; De Paola et al., 2011; Ferri et al., 2011;

Fondriest et al., 2013; Han et al., 2010a; Han et al., 2011; Kitajima et al., 2010; Smith et al., 2013; Tisato et al., 2012; Yao et al., 2013a). The onset of dynamic weakening in experiments performed with blocks of granite (Reches and Lockner, 2010) was attributed to wear of the solid rock material, formation of a gouge layer, and the development of a thin actively deforming zone (the "third body" of Reches and Lockner, 2010) that was suggested to lubricate the sliding surface. In the short-displacement experiments of Goldsby and Tullis (2011) and Kohli et al. (2011) the evolution of shear stress during slip acceleration and deceleration prompted the authors to suggest that flash heating and weakening occurred following strain localization in a thin gouge layer formed by wear between solid rock cylinders. More recently, Proctor et al. (2014) compared the frictional behavior of serpentinite gouges and solid rings (bare surfaces) of serpentinite. They found that higher slip velocities were required to initiate dynamic weakening in the gouges compared to the solid samples, and concluded that flash weakening in the gouges was delayed due to initially distributed deformation.

In general, the above experimental studies have shown that the presence of gouges is likely to be an important factor in the dynamic evolution of fault strength during seismic slip. This is in addition to the critical role played by gouges in determining the stability of faults during the nucleation phase of earthquakes (e.g. Beeler et al., 1996; Giger et al., 2008; Ikari et al., 2011; Logan et al., 1979; Mair and Marone, 1999; Marone, 1998; Marone et al., 1990; Niemeijer et al., 2008; Rathbun and Marone, 2010; Scholz, 2002; Scruggs and Tullis, 1998; Scuderi et al., 2013). However, most previous experimental studies performed at high-velocities have focused on gouge microstructure at the end of relatively large-displacement experiments, and thus the correlation between microstructure (e.g. strain localization) and mechanical behavior remains poorly understood.

The objective of the present paper is to report on an experimental and microstructural investigation of strain localization and its influence on dynamic weakening in granular calcite gouges. Calcite is an important, and in some cases dominant, mineral in many seismically active regions worldwide, where main shocks and aftershocks nucleate within and propagate through thick sequences of carbonates (Italy, e.g. 2009 Mw 6.3 L'Aquila earthquake, Chiarabba et al., 2009; Chiaraluce, 2012; Greece, e.g. 1995 Ms 6.6 Western Macedonia earthquake, Jackson, 1994; Himalayan orogenic belt, e.g. 2008 Mw 7.9 Wenchuan earthquake, Verberne et al., 2010). We employed a rotary-shear friction apparatus to deform layers of calcite gouge at high slip velocities and moderately high normal stresses. By tightly controlling the total experimental displacements, we systematically investigated the relationships between gouge mechanical behavior and microstructural evolution prior to and during the transition to dynamic weakening.

2. Methods

2.1 Sample preparation and starting materials

Experiments were performed with SHIVA (**S**low- to **Hi**gh-**V**elocity rotary-shear friction **A**pparatus; Fig 1a) at the INGV, Rome (Di Toro et al., 2010; Niemeijer et al., 2011) using a sample holder for incohesive materials (gouge) with rotary and stationary parts (Figures 1b,c). The rotary side of the gouge holder consists of a base plate (*a* in Figure 1b) and inner and outer rings (*g, i* in Figure 1b) that prevent gouge extrusion during the experiments. The inner and outer rings slide over a base disc (*h* in Figure 1a) located in the stationary base plate (*f* in Figure 1b). Both the rotary base plate and the stationary base disc have a crosshatch pattern of surface roughness where in contact with the gouge layer (Figure 1c; amplitude of surface roughness 400 µm, wavelength 800 µm). Axial load on the gouge layer is applied directly through the stationary base plate by the loading column of SHIVA (Di Toro et al., 2010). Axial load on the inner and outer sliding rings is modulated by five outer springs (*j* in Figures 1a,b) and one inner spring (*e* in Figure 1a). Calibration tests (Smith et al., 2013) indicate that the contribution to measured torque values from the sliding rings is negligible (<2.5% of measured torque) at the normal stresses used in these experiments (generally >8.5 MPa, two experiments at 4 MPa).

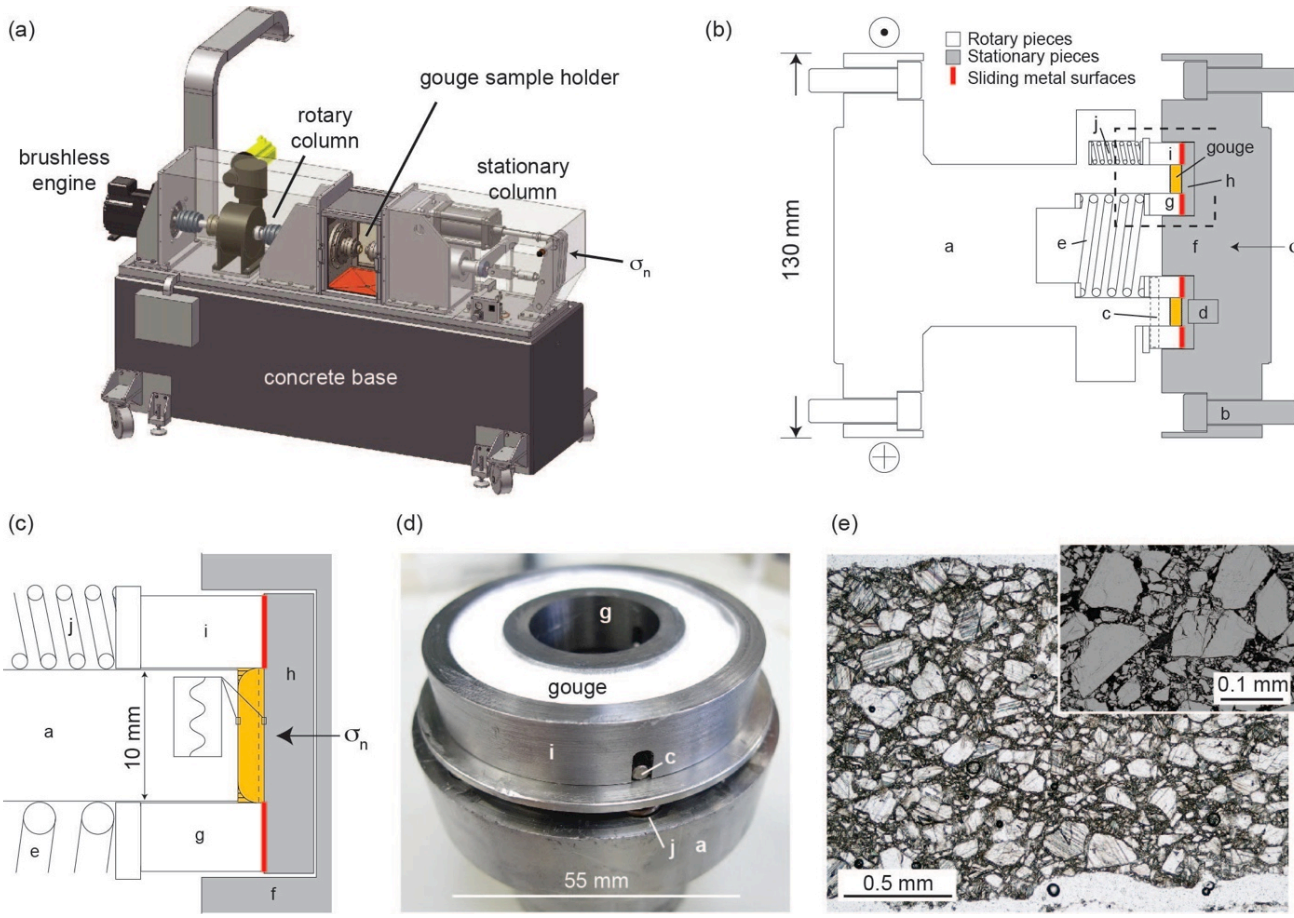

Figure 1: Experimental set-up and sample assembly for gouge experiments. **(a)** Photograph of the SHIVA apparatus with main components labeled as followed: - (b) Schematic diagram of gouge holder. Details of calibration tests can be found in the Supplementary Information of Smith et al. (2013). Labeled pieces of the gouge holder are: a, rotary base plate; b, mounting bolts; c, rotary driving pins; d, anti-rotation pins for base disc; e, inner spring; f, stationary base plate; g, inner sliding ring; h, stationary base disc; i, outer sliding ring; j, outer springs. The gouge layer is contained between the outer and inner rings that slide over the base disc (sliding contacts in red). Normal stress (σ_n) is applied to the gouge layer by the loading assembly behind the stationary column (Di Toro et al., 2010). Normal stress on the sliding rings is modulated by inner and outer springs. **(c)** Enlargement of part b showing

the gouge compartment of the sample holder [modified after Proctor et al., 2014]. The dashed line indicates the region where localization typically occurs in the gouge layers. The hatched areas in the corners of the gouge layer remain relatively undeformed due to the sample geometry (similar to the shielding effects discussed in (Beeler et al., 1996)). Where in contact with the gouge layer, the rotary and stationary pieced have a cross-hatched pattern of surface roughness with wavelength 800 μm and amplitude 400 μm. (d) Photograph of calcite gouge layer (35/55 mm int./ext. diameters) prior to an experiment. Labeled pieces are defined in part a. A thin layer of high-temperature grease is applied to the sliding surfaces of the rings to reduce friction. **(e)** Optical photomicrograph in plane polarized light (main image) and backscattered scanning electron microscope detail of calcite gouge compacted to 15 MPa. The starting material has a grain size <250 μm. During initial compaction, some fracturing and twinning of calcite grains occurs.

The gouge starting material was prepared by grinding fragments of Carrara marble in a pestle and mortar. The gouge was passed through a 250-μm sieve and all particles that passed through the sieve were included in the starting gouge. Powder X-ray diffraction analysis together with Scanning Electron Microscope (SEM) observations indicate that the starting material is composed of >99 wt% calcite, with <1 wt% dolomite, quartz, and muscovite as accessory phases (typical minor phases in Carrara marble: Smith et al., 2013). Each experiment used 5 g or 3 g of calcite gouge, resulting in ring-shaped gouge layers (35/55 mm int./ext. diameters; Figures 1b-d) with initial thicknesses of, respectively, c. 3 mm and c. 2 mm (Figures 1b-d).

2.2 Experimental and analytical procedures

All of the experiments were performed under room-dry conditions (room humidity varied between 50% and 80%). Each experiment consisted of the following steps: 1) preparation of the gouge layer following the procedures outlined in Section 2a; 2) mounting of the gouge sample holder in SHIVA and loading of the gouge layer to the target normal stress; 3) deformation of the gouge layer under the desired conditions of maximum slip velocity, acceleration and deceleration rate, and total displacement; and, 4) unloading and recovery of the deformed gouge layer for microstructural analysis. Experiments were performed at constant normal stresses of 4 – 26 MPa and maximum slip velocities up to 3.4 m s^{-1}. Total displacement in each experiment was controlled precisely using two digital encoders located on the rotary column. One encoder with an angular resolution of x μm was used to control and measure displacements up to 0.01 m. The second encoder with a lower angular resolution of x μm was used to control and measure displacements greater than 0.01 m. Axial displacements were measured using a Linear Variable Differential Transformer (LVDT). Experimental data (e.g. axial load, torque, axial displacements, angular rotation) were acquired at a frequency up to 25 kHz, and determination of total displacement, slip rate, and shear stress followed methods outlined in Di Toro et al. (2010).

Two types of experiment were performed on calcite gouges: single-slide experiments and slide-hold-slide experiments. In single-slide experiments, only one slip pulse was imposed on the gouge layer before it was recovered for microstructural analysis. In slide-hold-slide experiments, two slip pulses were imposed under identical conditions, separated by a hold period lasting x-x seconds during which the normal stress was held constant and no angular movements of the rotary column were detected.

Following most of the experiments, the deformed gouge layers were cohesive and flinty, and could be recovered quite easily for microstructural analysis. Fragments of the gouge layers were impregnated under vacuum using low-viscosity epoxy, and petrographic sections cut perpendicular to the gouge layers and approximately parallel to the slip direction were prepared for microstructural observations using a transmitted-light petrographic microscope and a Zeiss Sigma VP Field-Emission Scanning Electron Microscope (SEM; in the Otago Centre for Electron Microscopy, University of Otago) operating in backscattered mode (acquisition conditions: accelerating voltage 15 kV, working distance 6-8.5 mm). Energy-dispersive X-ray Spectroscopy (EDS) on the SEM was used to produce the element distribution map in Figure 6b.

2.3 Experiments with solid cylinders (bare surfaces) of marble

To compare the mechanical behavior of calcite gouges to solid rocks (i.e. bare surfaces) of the same mineralogical composition, single-slide experiments were performed on hollow cylindrical samples (30/50 mm int./ext. diameter) of Carrara marble. Each experiment used newly prepared cylindrical samples. The bare sliding surfaces were ground with 320 grit sandpaper before each experiment. The experimental procedures for the Carrara marble cylinders were the same as those detailed above, except that a different sample holder was used to grip the solid cylinders (sample procedures for solid cylinders described in Di Toro et al., 2010; Niemeijer et al., 2011; Violay et al., 2013).

3. Results

3.1 Dynamic weakening in calcite gouges and bare surfaces

Figure 2a shows the evolution of shear stress and slip velocity for two representative slide-hold-slide experiments performed at 8.5 MPa normal stress on (i) a 2 mm-thick layer of calcite gouge (red data, s753) and (ii) bare surfaces of calcite marble (grey data, s758). Slip is reported on a log scale to highlight the mechanical behavior in the early stages of slip. For clarity, only the slip velocity data for the gouge experiment are shown, but the slip velocity evolution was nearly identical in both experiments. Each slide had 2 m of displacement, a maximum slip velocity of 2.25 m s^{-1}, and acceleration and deceleration rates of 7 m s^2. The slides were separated by a static hold period of 40 seconds. Figure 2b shows variations in axial displacement during the two experiments, where positive changes indicate axial shortening and negative changes indicate dilation.

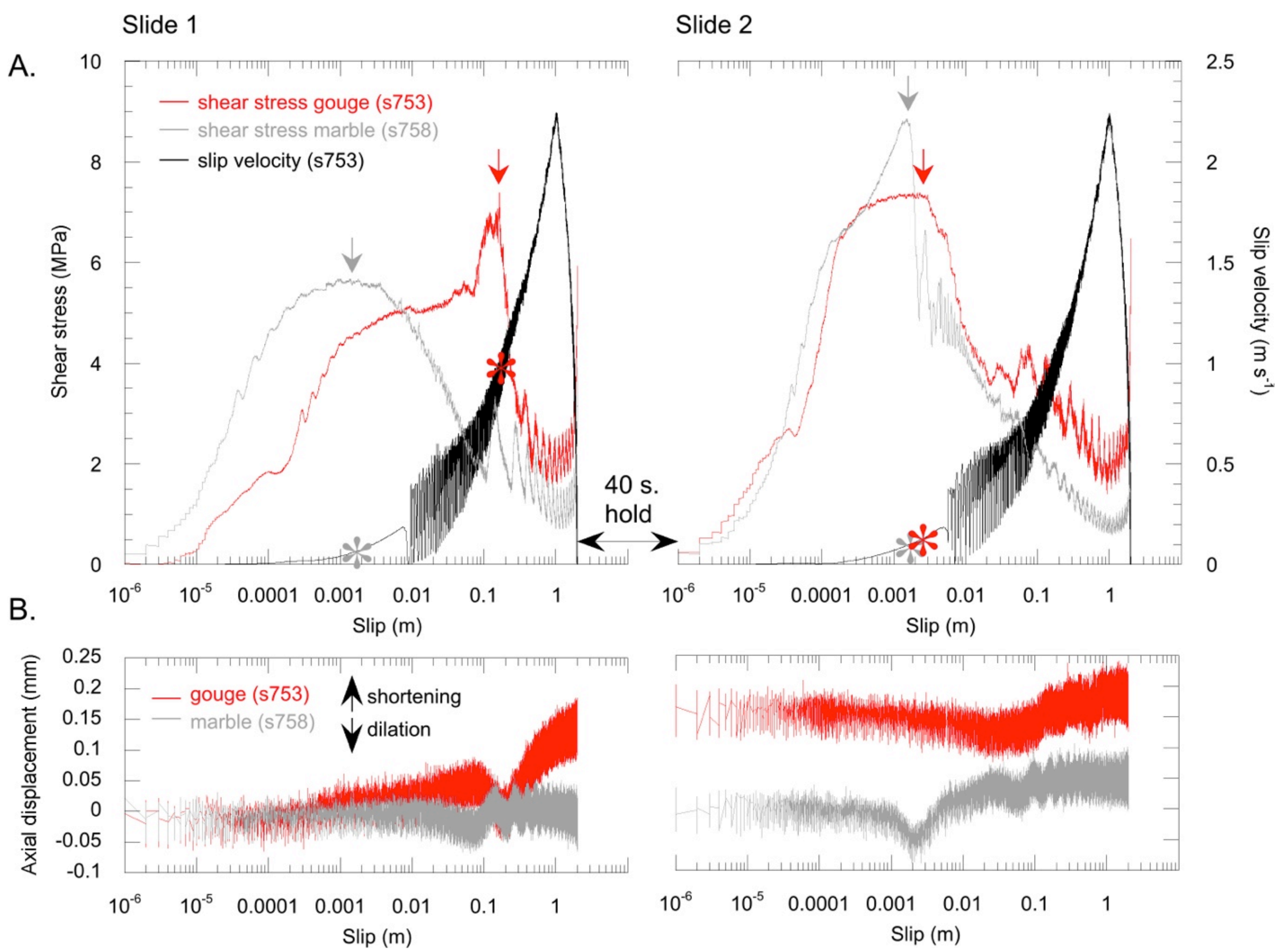

Figure 2: Evolution of shear stress, slip velocity and axial shortening during slide-hold-slide experiments on calcite gouge (s753) and bare surfaces of calcite marble (s758). Experiments were performed under identical conditions (8.5 MPa normal stress; 2.25 m s^{-1} maximum slip velocity; acceleration and deceleration of 7 m s^2; 2 m displacement during each slide; slides separated by a static hold period of 40 seconds). On the curves of shear stress and axial displacement, the systematic oscillations in the data (spaced every c. 0.125 m in the marble experiments and c. 0.15 m in the gouge experiments) are due to small misalignments between the solid marble cylinders or small variations in

gouge layer thickness. **(a)** Slide 1: the onset of weakening in calcite marble (grey arrow) occurred after c. 0.002 m of slip at a slip velocity of c. 0.1 m s^{-1} (grey star on slip velocity curve). Instead, the calcite gouges showed a prolonged phase of strengthening prior to peak shear stress and dynamically weakened (red arrow) after ~0.2 m of slip at a much higher slip velocity of ~1 m s^{-1} (red star on slip velocity curve). Slide 2: the onset of weakening in both calcite marble and calcite gouge occurred after ~0.002 m of slip at a slip velocity of ~0.1 m s^{-1}. **(b)** During slide 1, axial shortening was negligible in the calcite marble, but a significant phase of dilation occurred in the calcite gouge layer prior to peak stress (between 0.1 – 0.2 m slip). Dilation ended in the gouge layer at peak stress and was followed by compaction of ~150 μm. During slide 2, ~50 μm of further compaction took place in the calcite gouge layer after ~0.05 m of slip. In the calcite marble, a short phase of dilation lasting ~1 mm was recorded just prior to peak stress (between 0.001 – 0.002 m).

These two experiments illustrate significant differences in the mechanical behavior of calcite gouge layers and bare surfaces at seismic slip rates. During slide 1, the calcite marble initially strengthened reaching peak shear stress (5.5 MPa) after c. 0.002 m of slip (approximated by grey arrow in Figure 2a). The marble then dynamically weakened to a much lower shear stress of 1 MPa after c. 1 m of slip. Dynamic weakening in the marble initiated at a slip velocity of c. 0.1 m s^{-1} (see grey star on slip velocity curve in Figure 2a).

No significant axial displacements were recorded during slide 1 with the marble cylinders (Fig 2b). The oscillations observed in the axial displacement data (and the corresponding shear stress data) for the marbles are systematically spaced every c. 0.125 m, which corresponds to the average circumference of the solid marble cylinders. The oscillations in these data are thought to reflect a small misalignment between the rotary and stationary columns of the deformation apparatus, or slightly non-parallel sliding surfaces of the marble samples.

In comparison to the marble, the calcite gouge showed a prolonged phase of strengthening at the start of slide 1 (Figure 2a). Dynamic weakening in the gouge initiated after c. 0.2 m of slip (approximated by red arrow in Figure 2a) at a slip velocity of c. 1 m s^{-1} (see red star on slip velocity curve in Figure 2a). The minimum shear stress obtained by the gouge layer following dynamic weakening was slightly higher than in the solid marble samples (Figure 2a). The gouge layer initially shortened by ~50 µm, then between 0.08 – 0.2 m a transient phase of dilation was recorded (~100 µm dilation; Figure 2b). Dilation ended once peak shear stress was reached in the gouge layer, upon which renewed shortening occurred. Overall shortening of c. 150 µm was recorded in the gouge layer during slide 1 (Figure 2b).

During slide 2, the evolution of shear stress was similar in both the calcite marble and calcite gouge (Figure 2a). In both experiments, dynamic weakening initiated after c. 0.002 m of slip (grey and red arrows in Figure 2a) at a slip velocity of c. 0.1 m s^{-1} (grey and red stars on slip velocity curve in Figure 2a). The decay from peak to minimum shear stress occurred over roughly the same slip distance in both experiments, although as observed in slide 1 the minimum shear stress obtained by the gouge layer was slightly higher than the solid marble cylinders (Figure 2a).

Axial displacements during slide 2 in the gouges were relatively minor compared to slide 1, although ~50 µm of additional shortening took place after c. 0.03 m of slip (Figure 2b). At the start of the additional shortening during slide 2, there was a slight increase in shear stress, possibly reflecting minor gouge extrusion between the sliding rings. In the marble, a short-lived phase of dilation occurred between c. 0.001-0.002 m, just prior to peak shear stress (Figure 2b). Following peak shear stress, shortening of ~100 µm was observed.

Figure 3 summarizes the slip distance required to initiate dynamic weakening in calcite gouge layers (e.g. grey and red arrows in Figure 2.) and its dependence on normal stress and gouge layer thickness for 31 single-slide and slide-hold-slide experiments with an acceleration rate of 7 m s^2. Also shown are data from 13 single-slide experiments on solid cylinders (bare surfaces) of calcite marble. The main results can be summarized as follows (Figure 3):

i) During slide 1 in calcite gouges (red and green filled symbols) the initial strengthening phase lasts between c. 3-30 cm. The length of the strengthening phase decreases with increasing normal stress between 4 – 26 MPa, and it also decreases for thinner gouge layers. Above a normal stress of 15-20 MPa, the length of the strengthening phase may remain constant with increasing normal stress, although more data are required to confirm this.

ii) During slide 2 in gouges (red and green open symbols), the strengthening phase is much shorter, lasting on the order a few millimeters or less. The strengthening phase in slide 2 is independent of both normal stress and layer thickness.

iii) The length of the strengthening phase during slide 2 in gouges is comparable to that observed in solid cylinders of calcite marble (grey symbols) over the range of investigated normal stresses.

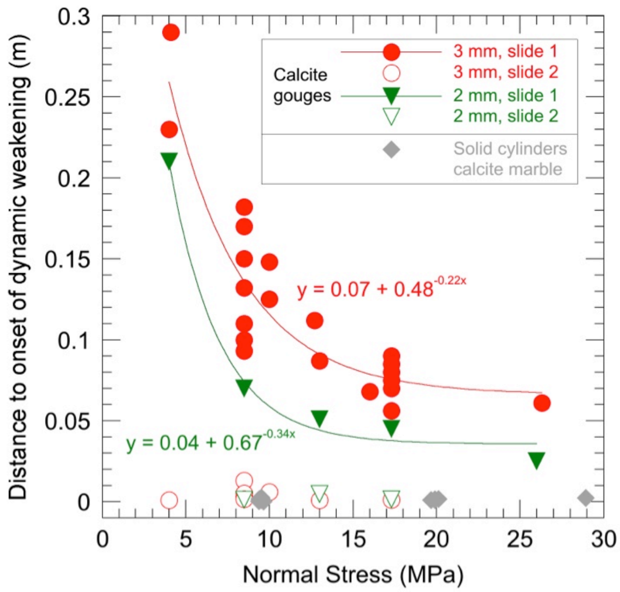

Figure 3: Distance to onset of dynamic weakening vs. normal stress for 31 single-slide and slide-hold-slide experiments performed on 2- or 3-mm thick layers of calcite gouge, as well as 13 single-slide experiments on solid cylinders (bare surfaces) of calcite marble. In all experiments the acceleration and deceleration rates were 7 m s^2. The data for slide 1 in gouges are approximated using best-fit exponential decay functions (R^2 = 0.81 for 3 mm thick layers, R^2 = 0.99 for 2 mm thick layers).

3.2 Velocity dependence and hysteresis

In experiments on calcite gouge, a marked hysteresis effect was observed in plots of shear stress versus slip velocity. Figure 4 shows shear stress versus slip velocity for a representative slide-hold-slide experiment (s363) performed on a 3 mm-thick layer of calcite gouge (σ_n = 8.5 MPa, maximum slip velocity 1 m s^{-1}, each slide 2 m of displacement). As slip velocity increased at the start of slide 1 (red data), shear stress initially increased rapidly, followed by a prolonged phase of more gradual strengthening up to a slip velocity of c. 0.8 m s^{-1} (Figure 4). At c. 0.8 m s^{-1} rapid dynamic weakening occurred, with shear stress decreasing to much lower values as the maximum slip velocity (c. 1 m s^{-1})

was approached (Figure 4). During deceleration, shear stress increased roughly linearly with decreasing velocity and ultimately recovered to around 90% of its peak value. The rate at which shear stress recovered during deceleration was lower than the rate at which dynamic weakening proceeded, resulting in an overall clockwise path in shear-stress-velocity space (Figure 4).

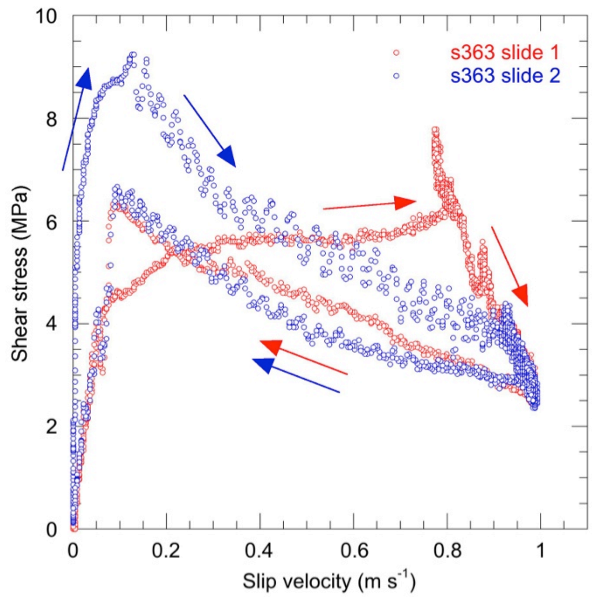

Figure 4: Hysteresis in shear stress data observed in a representative slide-hold-slide experiment (s363; 3 mm-thick calcite gouge layer, 8.5 MPa normal stress, 1 m s^{-1} maximum slip velocity, acceleration and deceleration 7 m s^2). The arrows indicate the sequence of data acquisition during acceleration and deceleration. During slide 1 (red data), dynamic weakening initiated at a relatively high slip velocity of ~0.8 m s^{-1}. During deceleration, shear stress increased again, but at a rate much lower than during dynamic weakening. During slide 2 (blue data), weakening initiated at a slip velocity almost an order of magnitude lower than slide 1 (~0.1 m s^{-1}), and the evolution of shear stress during acceleration and deceleration was similar (i.e. the hysteresis effect was much less pronounced than in slide 1).

During slide 2 (following a hold period of 42.6 seconds), the calcite gouge again strengthened rapidly as the slip velocity increased from zero, but dynamic weakening initiated at a much lower slip velocity of c. 0.1-0.15 m s^{-1} (Figure 4). Above this slip velocity, shear stress decreased to a minimum value comparable to that obtained in slide 1. During deceleration of slide 2, the shear stress recovered to around 70% of its peak value and followed a nearly identical path to slide 1 (Figure 4). Overall, the marked hysteresis that characterized the shear stress-velocity evolution of slide 1 was much less pronounced during slide 2.

3.3 Microstructural evolution of calcite gouge layers

A series of experiments was performed at 8.5 MPa normal stress with increasing total displacements in the range of 0.01-0.35 m to provide insights in to the microstructural evolution of the calcite gouge layers during the transition from strengthening to dynamic weakening. Observations from three of these experiments are summarized below (Figures 5,7,8). All three experiments were performed with 3 mm-thick gouge layers, imposing a target acceleration rate of 6 m s^2 and a target maximum slip velocity of 1.1 m s^{-1}. An additional small displacement (0.028 m) experiment was performed at a higher normal stress of 17.3 MPa in which a dolomite strain marker was constructed in the calcite gouge layer prior to shearing (Figure 6).

3.3.1 0.01 m slip (s784)

Due to the small displacement in this experiment the maximum slip velocity obtained was 0.27 m s^{-1} (Figure 5a). The total displacement was approximately an order of magnitude lower than the c. 0.1 m required for dynamic weakening under these experimental conditions (see experiment s493, grey curve, in Figure 5a and data in Figure 3 at 8.5 MPa). Axial shortening of c. 50 μm was measured after 0.01 m of slip (Figure 5a).

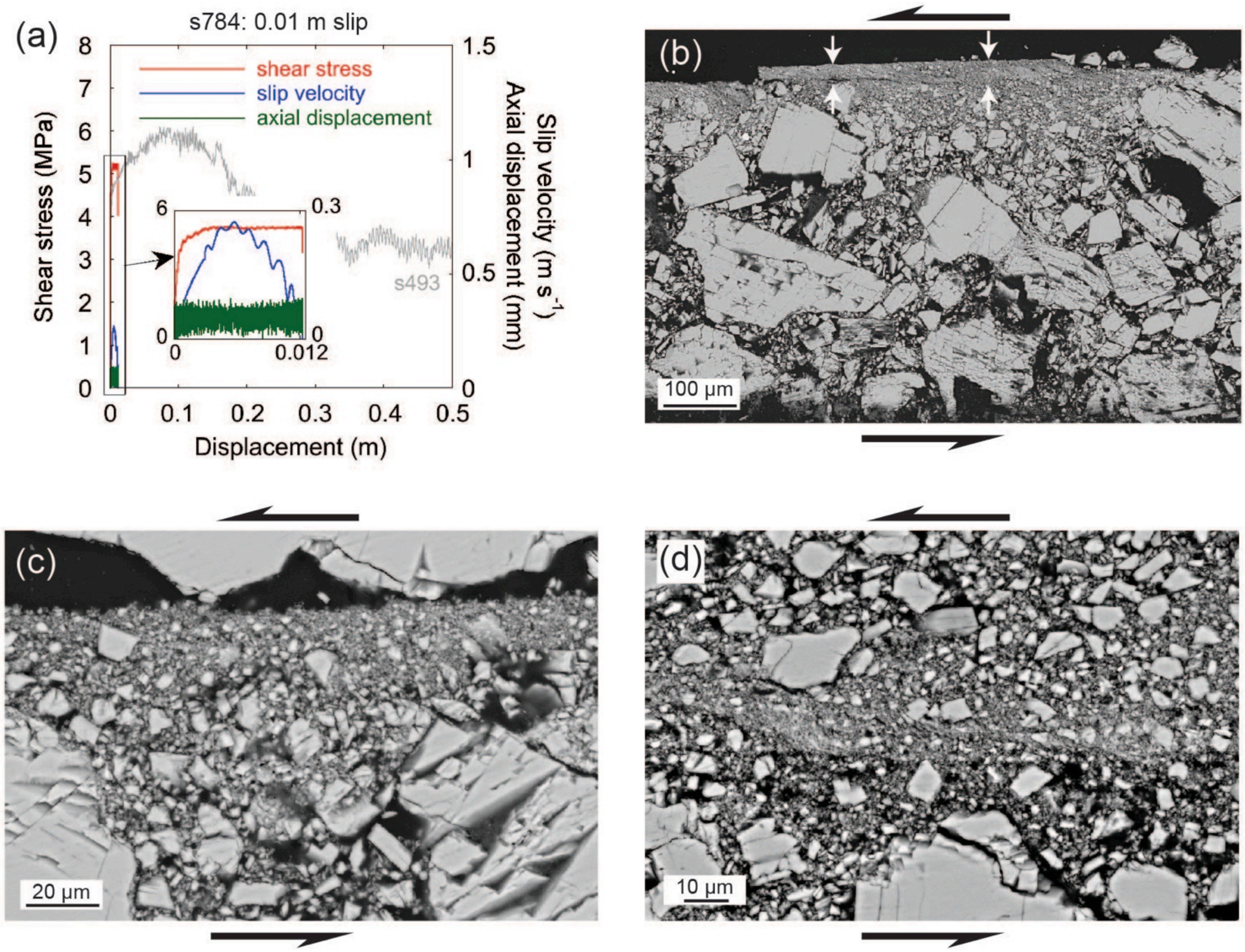

Figure 5: Mechanical data and microstructures of experiment s784, stopped after 0.01 m of slip. (a) Plot of shear stress, slip velocity and axial displacement vs. slip. The inset box shows a detail of the first 0.01 m of slip. The grey curve (also in Figures 7, 9, 10) shows the shear stress evolution of experiment s493, performed under identical conditions but taken to a total displacement of 1 m. (b) SEM image of gouge layer. A narrow shear band of fine grain size (outlined by the white arrows) is developed close to the stationary side of the gouge holder (see approximate position in Figure 1c). The bulk of the gouge layer is much coarser grained and resembles the starting material. (c) Detail of fine-grained shear band showing angular calcite clasts < 10 μm in size embedded within a much finer-grained calcite matrix. The shear band is < 20 μm thick. Larger clasts outside the shear band are

heavily fractured along cleavage planes. (d) Some parts of the shear band contain domains of particularly fine grain size, appearing as lighter patches on SEM images. The example shown here is c. 10 µm wide and 100 µm long and runs sub-horizontally across the middle of the image.

The calcite gouge layer contains a well-defined shear band up to 20 µm thick (between white arrows in Figure 5b), defined in SEM images by a much finer grain size and more compact appearance compared to the surrounding gouge layer (Figures 5b,c). The grain sizes and overall appearance of the bulk of the gouge layer (i.e. outside the slip zone) are similar to the gouge starting material (compare Figures 1e and 5b). As observed in all gouge experiments that reached slip velocities >0.1 m s^{-1}, the shear band developed sub-parallel to gouge layer boundaries (i.e. a Y-shear (Logan et al., 1979)) and at a distance of c. 100 µm from the surface roughness on the stationary side of the gouge holder (see position of dashed line in Figure 1c). The shear band consists of angular to sub-angular calcite grains < 10 µm in size that are surrounded by a finer-grained calcite matrix (Figure 5c). Internally, the shear band contains elongate domains (up to 100 µm long and 10 µm wide) of extremely fine grain size aligned sub-parallel to the shear band boundaries (Figure 5d).

3.3.2. Strain distribution before the transition to dynamic weakening

Experiment s781 was performed at a higher normal stress of 17.3 MPa (Figure 6) and stopped after 0.028 m of slip. At this normal stress the onset of dynamic weakening in calcite gouge occurs after 0.05 – 0.1 m of slip (see example of s626, grey curve, in Figure 6a and data in Figure 3). The maximum slip velocity reached in s781 was 0.4 m s^{-1} and overall c. 50 µm of axial shortening was measured (Figure 6a).

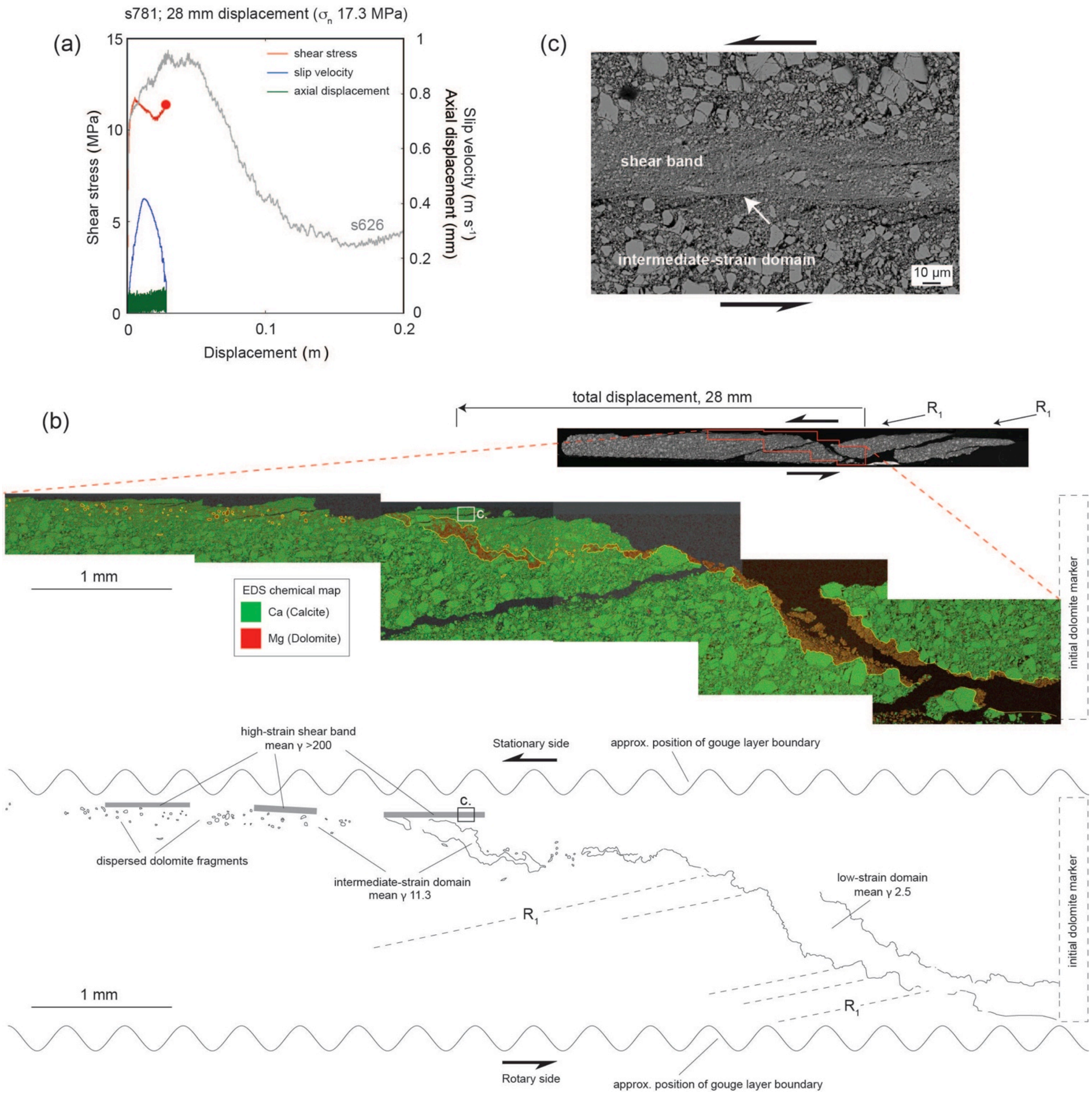

Figure 6: Experiment s781 (17.3 MPa normal stress) performed with a dolomite strain marker and stopped after 0.028 m of slip. **(a)** Evolution of shear stress, slip velocity and axial displacement in experiment s781. Also shown is the shear stress evolution in experiment s626 (grey curve) performed under identical conditions. Experiment s626 indicates that the onset of dynamic weakening under these conditions occurs after ~0.05 m of slip (also see data in Figure 3). **(b)** SEM-EDS images of the calcite

gouge layer and dolomite strain marker. The greyscale image shows an SEM mosaic of the entire gouge layer and a representation of the total experimental displacement. The colored image shows an EDS chemical map of Mg (dolomite) and Ca (calcite) distribution in the gouge layer that was used to reconstruct the strain distribution after shearing. The dolomite marker was initially sub-perpendicular to gouge layer boundaries. The lower line drawing shows a tracing of the dolomite strain marker and an interpretation of the three strain domains distinguished from the geometry of the marker. A series of R_1-Riedel shears offset the edges of the strain marker in the low-strain domain. **(c)** SEM image (location shown in part b) of the high-strain shear band. The shear band is 50-100 μm wide and much finer grained than the adjacent gouge. The white arrow shows where one edge of the shear band is defined by a discrete surface.

Prior to the experiment, a c. 300 μm-wide "wall" of relatively fine-grained (particle size fraction <63 μm) dolomite gouge was constructed approximately perpendicular to the slip direction and gouge layer boundaries to act as a strain marker (Figure 6b). Dolomite is distinguished in the EDS chemical map shown in Figure 6b by a red color (corresponding to Mg) and calcite by a green color (corresponding to Ca). The geometry of the dolomite strain marker reveals a number of significant microstructures within the gouge layer and it can also be used to broadly define three strain "domains". From the rotary to the stationary side the three domains are (Figure 6b):

(1) A low-strain domain c. 1.5 mm thick that accommodated c. 3.8 mm of slip. The mean shear strain (γ) in this domain (calculated as slip/thickness) is c. 2.5. The grain sizes in this domain are comparable to the gouge starting material (e.g. Figure 1e). The edges of the strain marker are intact and roughly parallel, and there is little or no mixing between the dolomite marker and the surrounding calcite gouge. However, the edges of the marker are offset by a number of R_1-Riedel shears defined by bands

of grain size reduction and open fractures (the latter assumed to have formed by normal stress unloading). The Riedel shears lie at angles of 15-20° to the gouge layer boundaries and have measured synthetic (i.e. the same as the bulk shear sense) offsets of 100-200 μm.

(2) An intermediate-strain domain c. 0.4 mm thick that accommodated c. 4.5 mm of slip. In this domain mean γ is 11.3, the dolomite strain marker is heavily disrupted, and there is some mixing between the dolomite and calcite gouges. In the region closest to the high-strain shear band (see below) the dolomite marker becomes increasingly disrupted to form a layer containing only dispersed dolomite fragments.

(3) A high-strain shear band between 50 - 100 μm thick that accommodated up to 19.7 mm of slip (total experimental slip of 28 mm minus the slip in the low- and intermediate-strain domains), resulting in mean $\gamma > 200$. SEM analysis indicates that both boundaries of the high-strain shear band are defined by an abrupt reduction in grain size and, in places, more discrete surfaces (Figure 6c). It is not possible to estimate how much displacement occurred in the sliver of calcite gouge lying between the shear band and the stationary side of the gouge holder, and hence the estimate of 19.7 mm displacement for the shear band is a maximum estimate. However, given the relatively coarse grain size preserved in the sliver (Figure 6c; comparable to the intermediate-strain domain) the displacement is considered to be minor. Within the high-strain shear band, the dolomite strain marker is completely disaggregated, although in the slip direction small grains of dolomite derived from the strain marker can be found dispersed throughout. Internally, the shear band contains diffuse layering defined mainly by pockets of slightly coarser-grained gouge (Figure 6c). Within and surrounding the shear band, calcite grains are cut by intergranular fractures (Figure 6c).

3.4.3. 0.2 m slip (s631)

Experiment s631 was stopped after 0.2 m of slip (Figure 7a). During deceleration the shear stress recovered to nearly its peak value. Comparison to other experiments performed under the same conditions (e.g. s493, grey curve, in Figure 7a; data in Figure 3) indicates that s631 was stopped approximately mid-way through the dynamic weakening phase. A total of c. 200 μm of axial shortening was recorded, although this included a transient phase of dilation between c. 0.05-0.12 m (Figure 7a). Dilation ended once peak shear stress was reached and dynamic weakening initiated.

Compared to experiments stopped before the onset of dynamic weakening (e.g. Figures 5,6), the bulk of the gouge layer has a much finer grain size (Figure 7b), indicating that some distributed deformation and grain size reduction occurred even after the high-strain shear band had formed. The shear band in this experiment is up to 100 μm wide (between white arrows in Figure 7b), similar to that observed at an earlier stage in the strain history (i.e. s781 in Figure 6). The shear band contains sub-angular to sub-rounded calcite grains <10 μm in size (Figure 7c). The most significant difference in the microstructure of the shear band compared to pre-peak stress is that it contains many short (<100 μm) isolated slip surfaces that are sub-parallel to the shear band boundaries (Figure 7c). SEM observations show that thin (<10 μm) and elongate (<100 μm) regions of extremely fine-grained (<1 μm) and tightly packed calcite aggregates surround each slip surfaces (Figures 7c,d). Within these regions individual grains or grain boundaries cannot be recognized (Figure 7e). The fine-grained regions are commonly cut by small brittle fractures oriented at high angles to the shear band boundaries and showing micron-scale offsets (white arrows in Figure 7c). These fractures are assumed to have formed late in the experiments (during deceleration) or during sample preservation, suggesting that the short slip surfaces and surrounding fine-grained regions are more cohesive than the shear band matrix.

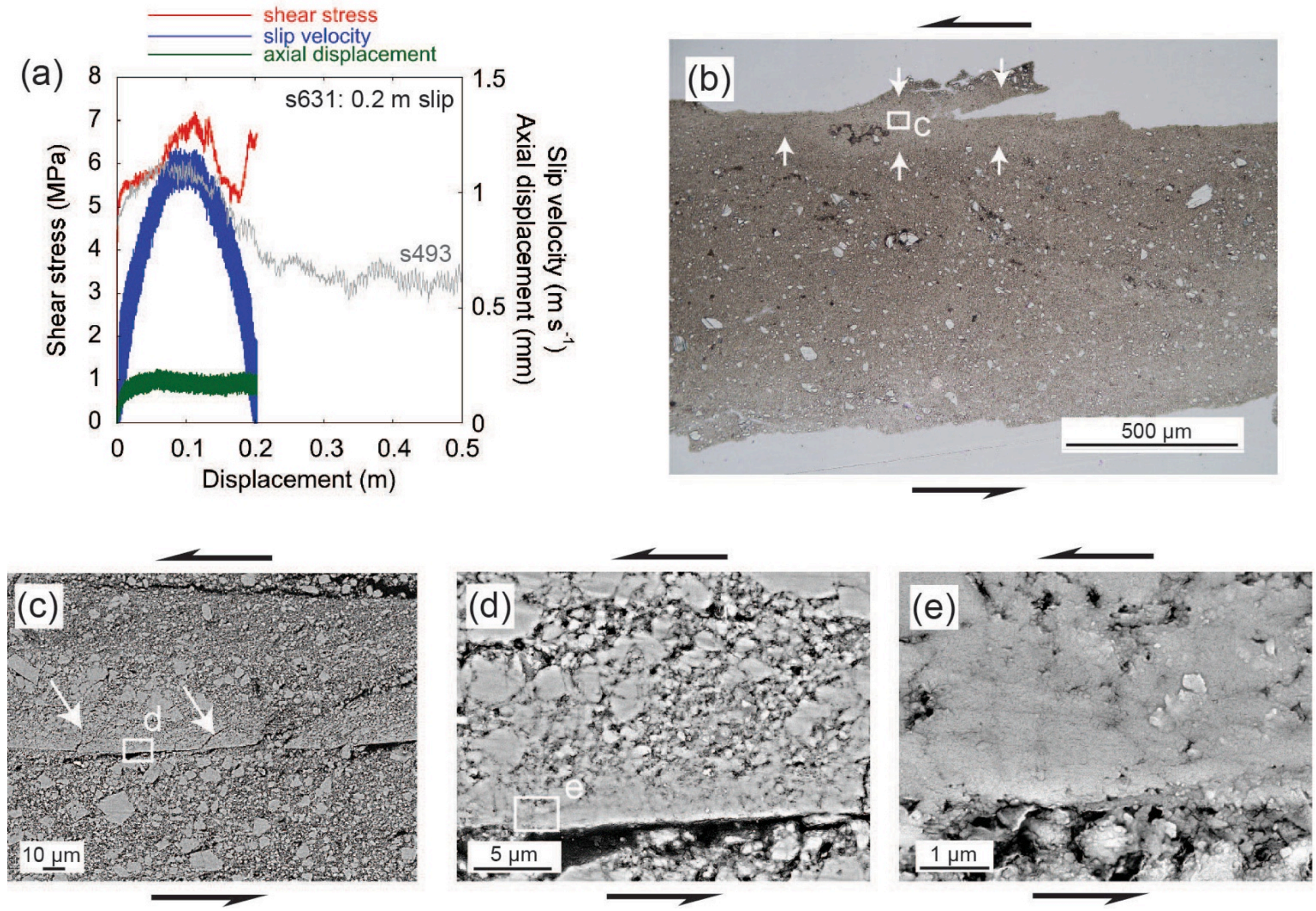

Figure 7: Mechanical data and microstructures of experiment s631, stopped after 0.2 m of slip. (a) Plot of shear stress, slip velocity and axial displacement. Comparison with s493 indicates that the experiment was stopped approximately mid-way through the dynamic weakening phase. Transient dilation of the gouge layer occurred during the strengthening phase, and ended once peak shear stress was reached. (b) Optical photomicrograph in plane-polarized light showing the fine-grain size of the bulk gouge layer and the c. 100-µm wide shear band (between white arrows). (c) SEM image of the shear band showing two discrete slip surfaces associated with regions of extremely fine grain size and low porosity. Small cracks with micron-scale offsets are indicated by white arrows. (d) Detail of one of the slip surfaces in part c. The slip surface is flanked by regions up to 10 µm wide in which the grain size is < 1 µm and the porosity is low compared to the surrounding shear band matrix. (e) Detail of d at

high magnification showing the extremely fine-grained and tightly-packed nature of the calcite aggregates. Individual grains or grain boundaries cannot be recognized.

3.4.4. 0.35 m slip (s492)

Experiment s492 was stopped after 0.35 m of slip, at the end of the dynamic weakening phase (i.e. as the shear stress reached "steady state" values; Figure 8a). A transient phase of dilation was recorded during the strengthening phase, which ended once peak shear stress was reached.

After 0.35 m of slip, the fine-grained shear band that formed at shorter displacements is cut by a single, continuous and relatively planar slip surface (delineated by white arrows in Figures 8b,c) along which the gouge layer parted during sample recovery. When removed from the sample holder, the slip surface was extremely cohesive, had flinty fracture, and reflected natural light in a specular way. In the petrographic microscope, the slip surface appears as a discrete fracture <2-3 μm wide cutting the surrounding fine-grained shear band (Figure 8c). Adjacent to the slip surface is a layer c. 10 μm thick that has a uniform color when observed with the sensitive-tint (gypsum) plate inserted in the petrographic microscope, suggesting that it has a crystallographic-preferred orientation (CPO; Figure 8c inset). There are also small, tabular fragments with a CPO in the surrounding shear band (e.g. yellow arrow in Figure 8c inset), interpreted as pieces of cohesive slip surface material that were broken off and reworked during slip. SEM observations of the material coating the 2-3 μm-wide slip surface show aggregates of highly elongate grains with irregular, rounded to lobate grain boundaries (Figure 8d). The grains are a few tens to a few hundreds of nanometers long and consistently aligned in the direction of shear, forming a well-defined shape-preferred orientation at an angle of c. 20° to the slip surface (measured clockwise in Figure 8d). The shear band material with a CPO adjacent to the slip surface is formed of calcite grains up to 1 μm in size with well defined, straight to slightly curved grain boundaries and roughly polygonal grain shapes (Figure 8e). Boundaries between adjacent grains commonly meet at triple junctions with interfacial angles of c. 120° (Figure 8e). As the slip surface is approached, the grains in this layer become smaller (<500 nm close to the slip surface) and develop more elongate grain shapes (Figure 8e). The grains closest to the slip surface are aligned in the shear direction and possess a shape-preferred orientation at an angle of c. 20° to the slip surface (Figure 8e).

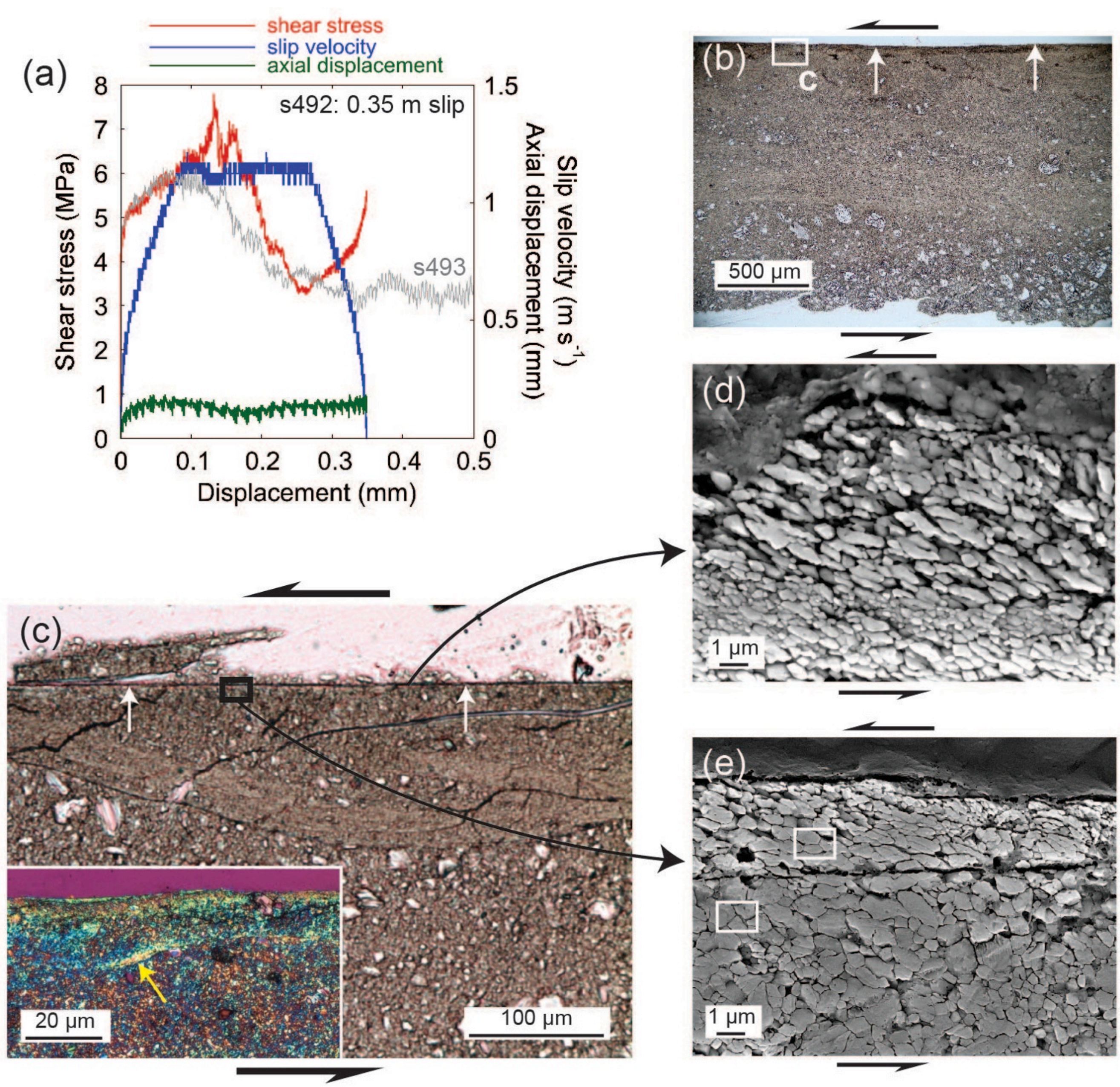

Figure 8: Mechanical data and microstructures of experiment s492, stopped after 0.35 m of slip. (a) Plot of shear stress, slip velocity and axial displacement. This experiment was stopped at the end of the dynamic weakening phase. (b) Optical photomicrograph in plane polarized light showing a single, discrete slip surface (marked by white arrow). (c) Detail of part b showing the discrete, 2-3-μm wide slip surface (white arrows) surrounded by the extremely fine-grained shear band. The inset shows an image of the slip surface and adjacent shear band with the sensitive-tint (gypsum) plate inserted in to the petrographic microscope. The uniform yellow and blue colors in a layer c. 10 μm thick immediately adjacent to the slip surface indicate the presence of a crystallographic-preferred orientation (CPO). Small tabular fragments with a CPO (yellow arrow) are also found in the shear band, probably representing pieces of cohesive slip surface material broken off and reworked during shear. (d) SEM image of the material coating the 2-3-μm wide slip surface. The elongate grains coating the slip surface are on the order of tens to hundreds of nanometers in size. (e) SEM image of the shear band layer containing a CPO. In this layer, calcite grains are micron-sized and have straight to slightly curved grain boundaries that often meet at grain triple-junctions (two examples in white boxes).

4. Discussion

4.1 Strain localization and dynamic weakening in calcite gouges

Both calcite gouges and solid cylinders (bare surfaces) of calcite marble experience dynamic weakening at moderate normal stresses (4 – 26 MPa) and slip velocities between ~0.1 – 1 m s^{-1}. However, much higher displacements and slip velocities are required to initiate dynamic weakening in the gouge layers. At the highest normal stresses investigated here (26 MPa), the displacement and slip velocity at the onset of dynamic weakening in 2-3 mm thick calcite gouge layers are approximately an order of magnitude higher than for solid cylinders (bare surfaces) of calcite marble or calcite gouge layers re-sheared following a static hold period.

Microstructural observations of experiments stopped at different displacements indicate that during shearing at high velocity, strain is initially distributed across the full thickness of the gouge layer. Localization to a boundary-parallel, high-strain shear band occurs in <0.01 m of slip, even although dynamic weakening does not occur until higher displacements (e.g. 0.1-0.2 m at 8.5 MPa normal stress; Figure 3). The shear band is initially quite thin (<20 μm) but broadens with displacement during the strengthening phase until it is c. 100 μm thick around peak stress (similar to the observations in Yao et al., 2013a). Once formed, the shear band accommodates a majority of subsequent slip, although some distributed deformation must occur outside the shear band to explain the progressive grain size reduction observed in the bulk of the gouge layer. Prior to peak shear stress, the shear band is active at the same time as sets of R_1 - Riedel shears (stage 1, Figure 9). Given the prevalence of angular to sub-angular calcite grains within the shear band, and the occurrence of intergranular fracturing in the bulk of the gouge layer, cataclasis is likely to be the most important deformation process prior to peak shear stress.

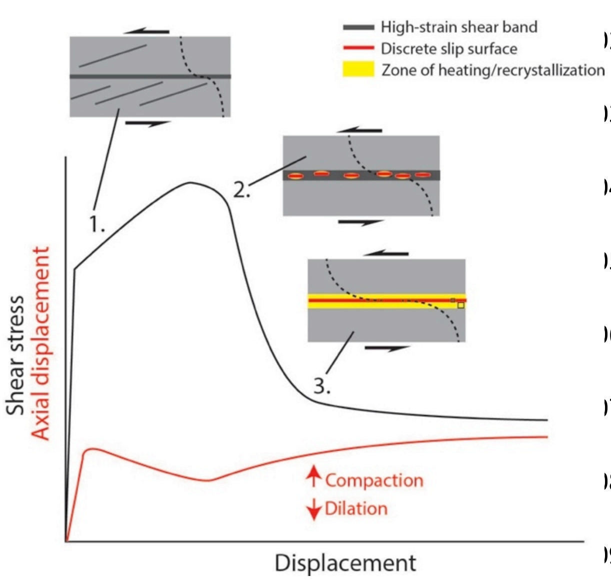

Figure 9: Schematic illustration of the mechanical and microstructural evolution of calcite gouge layers sheared at high velocity. 1: pre-peak stress, 2: peak stress, 3: end of dynamic weakening. Dashed lines approximate strain distribution.

The transition to dynamic weakening in calcite gouges is associated with a switch from layer dilation to compaction and the appearance of short and discontinuous slip surfaces within the boundary-parallel shear band (stage 2, Figure 9), each of which is surrounded by a region containing extremely fine-grained and tightly packed calcite aggregates. We interpret the slip surfaces and surrounding aggregates to represent zones of gouge in which the local slip velocities during shearing were high enough to allow frictional heating and welding of the extremely fine calcite grains. Welding is suggested on the basis that i) the aggregates around the slip surfaces have much lower porosity than the surrounding shear band matrix, ii) individual grains and grain boundaries cannot be recognized in the aggregates even at high magnifications, suggesting coalescence of sub-micron particles, and iii) the aggregates are cohesive enough to fracture, suggesting that individual particles are strongly bound to one another. In experiments performed under similar conditions to those applied here, Mitchell et al. (2014) detected CO_2 degassing from mixed calcite-dolomite gouge layers after less than 8 mm of displacement, before peak stress was reached. This indicates that temperatures in the gouge layers can locally reach the decomposition temperatures of carbonates (around 550°C for dolomite and 700°C for calcite; e.g. De Paola et al., 2011; Rodriguez-Navarro et al., 2009; Samtani et al., 2002) during the initial increments of shearing (Han et al., 2007). Given that carbonate decomposition temperatures are significantly higher than the c.180°C required for crystal-plastic deformation of calcite (e.g. Burkhard, 1990), the experimental results of Mitchell et al. (2014) support the assertion that welding of extremely fine-grained calcite aggregates could occur locally in the high-strain shear band after displacements corresponding to peak stress. Sawai et al. (2012) and Togo and Shimamoto (2012) interpreted grain welding to have occurred in high-velocity (<1.3 m s^{-1}) and large-displacement (up to 48 m) experiments on clay- and quartz-rich gouges on the basis of surface area measurements. In their experiments, gouge surface area decreased with increasing amounts of slip (and power density), suggesting particle aggregation during shearing. Accompanying microstructural analysis indicated that aggregation was probably due to welding of grain boundaries driven by the frictional heat produced in localized slip zones (Sawai et al., 2012; Togo and Shimamoto, 2012). Similar conclusions regarding grain welding as an active deformation process in high-velocity gouge experiments were recently published in Yao et al. (2013a,b).

By the end of dynamic weakening, deformation is fully localized, with the formation of a single 2-3-μm wide slip surface cutting the shear band (stage 3, Figure 9). The slip surface itself is coated with ultra-fine grains and is flanked by layers of calcite (Figures 8, 9) that have many of the microstructural characteristics (e.g. CPO and SPO; straight to slightly curved grain boundaries; grain-boundary triple junctions) of plastically-deformed and recrystallized calcite mylonites (e.g. Barnhoorn et al., 2004; Bestmann et al., 2000; Bestmann and Prior, 2003; Ebert et al., 2007; Herwegh and Kunze, 2002; Trullenque et al., 2006). Similar fabrics observed in high-velocity gouge experiments with total displacements >1 m have been attributed to recrystallization and grain growth caused by bulk frictional heating along the localized slip surface (Brantut et al., 2011; Fondriest et al., 2013; Han et al., 2010b; Kim et al., 2010; Ree et al., 2014; Smith et al., 2013; Yao et al., 2013b).

The microstructural evolution that we have documented in calcite gouges indicates that strain localization to a thin shear band is a critical precursor to dynamic weakening. Our observations are most compatible with dynamic weakening in calcite gouges resulting from a thermally triggered mechanism such as flash heating that requires both a high degree of strain localization and a minimum slip velocity (c. 0.1 m s^{-1}) to activate (Beeler et al., 2008; Goldsby and Tullis, 2011; Proctor et al., 2014; Rice, 2006).

4.2 Hysteresis in shear stress – velocity data

In the short-displacement experiments of Goldsby and Tullis (2011) and Kohli et al. (2011), performed on a range of solid rocks (granite, quartzite, novaculite, albite, gabbro, serpentine), the authors observed a hysteresis effect in shear stress-velocity data during acceleration and deceleration, similar to that observed in the present calcite gouge experiments (Figure 4). They concluded that during the initial stages of high-velocity sliding (and/or during the slow-velocity run-in phase in the case of Kohli et al. (2011)), a thin gouge layer (<40 μm) was quickly formed by wear of the solid rock surfaces. Because of this, up to several millimeters of slip were required to localize deformation within the gouge layer to such a degree that efficient heating could take place at grain contacts, leading to flash weakening (Goldsby and Tullis, 2011; Kohli et al., 2011). A marked hysteresis effect during high-velocity shearing of quartz-rich gouge layers at 0.56 MPa normal stress has also been noted previously by Sone and Shimamoto (2009).

Our experimental and microstructural observations, following those of Goldsby and Tullis (2011) and Kohli et al. (2011), suggest that the hysteresis observed in the calcite gouge data reflects progressive strain localization during acceleration to high velocity. In the slide-hold-slide experiments reported here, the hysteresis during the first slide is more pronounced than in the experiments of Goldsby and Tullis (2011) and Kohli et al. (2011) because of the relatively thick starting gouge layers (2-3 mm in these experiments as opposed to wear of bare rock surfaces producing gouge layers less than tens of microns thick in the case of Goldsby and Tullis (2011) and Kohli et al. (2011)). However, during the second slide the calcite gouge layers show much faster dynamic weakening, similar to solid cylinders of calcite marble. Based on microstructural observations, a possible explanation for this mechanical behavior is that deformation during the second slide is quickly localized to the discrete slip surface that forms by the end of dynamic weakening in slide 1 (e.g. stage 3 in Figure 9). Reactivation of the discrete slip surface during the second slide would reduce the effective gouge layer thickness to a few microns at most, explaining why the re-sheared gouge layers behave in a similar manner to solid cylinders of calcite marble. This mechanism is supported by SEM observations that show the microstructure of gouges deformed in slide-hold-slide experiments is essentially identical to that at the end of the dynamic weakening phase in single-slide experiments (e.g. stage 3 in Figure 9), the only notable difference being a thicker zone of gouge recrystallization adjacent to the slip surface. Further to this, multiple slip surfaces and reworked fragments of slip surface were not identified in the microstructure of slide-hold-slide experiments, suggesting that distributed deformation did not occur in the gouge layers at the start of slide 2.

4.3 Implications

In natural fault zones, the mechanical properties of fresh gouge layers (i.e corresponding to slide 1 in our experiments) are likely to be most relevant during seismic slip because of dynamic formation of gouge ahead of the rupture tip. Reches and Dewers (2005) showed that a mode II rupture propagating at 98% of the Rayleigh speed will result in tensile stresses of up to 3 GPa and volumetric strain rates exceeding 10^5 s^{-1} in the few millimeters around the rupture tip. Due to such intense stress (and temperature) pulses the fault rocks surrounding the rupture tip are expected to pulverize (Reches and Dewers, 2005; Sammis and Ben-Zion, 2008). Observations made in underground mines closely following small (<M2.2) shallow-focus earthquakes support the idea that layers of fine-grained gouge ("rock flour") can be dynamically generated (e.g. Heesakkers et al., 2011; Stewart et al., 2001). Additionally, the interaction of fault surface asperities during seismic slip will result in the formation of fresh gouge (Candela et al., 2009; Griffith et al., 2010; Power et al., 1987; Power et al., 1988; Sagy and Brodsky, 2009; Sagy et al., 2007). This means that even in granular fault rocks that have been recrystallized or cemented during the interseismic period (e.g. Bruhn et al., 1994; Gratier and Gueydan, 2007; Sibson, 1987; Tenthorey and Cox, 2006), strain localization in fresh gouge layers is likely to be a fundamental process controlling the dynamic strength of faults during seismic slip.

5. Conclusions

Calcite gouges deformed at seismic slip velocities show initial strengthening behavior before the onset of dynamic weakening. In fresh gouges, dynamic weakening occurs more rapidly at higher normal stresses and in thinner gouge layers. In gouges re-sheared following a hold period, dynamic weakening is much faster and mimics the behavior of solid cylinders of calcite marble. Microstructural observations show that localization to a high-strain shear band c. 100 μm wide is a critical precursor to dynamic weakening. Specifically, dynamic weakening is triggered by the formation of short slip surfaces in the shear band that we have interpreted as regions of local heating. Continued localization during dynamic weakening forms a through-going principal slip surface along which bulk frictional heating results in gouge recrystallization. If fresh gouge layers are formed dynamically at the rupture tip or due to asperity interaction during the first increments of seismic slip, a significant amount of displacement may be required to overcome the initial strengthening behavior and transition to dynamic weakening.

Acknowledgements

Elena Spagnuolo contributed the data on solid cylinders of calcite marble. Michele Fondriest, Tom Mitchell, Brooks Proctor and John Platt are thanked for constructive discussions on gouge deformation. Kat Lilly and Marco Brenna provided assistance with the SEM in the Otago Centre for Electron Microscopy (OCEM) at the University of Otago. The authors acknowledge funding from European Union Starting Grants (projects USEMS and NOFEAR to Di Toro) and a 2014 University of Otago Research Grant (to Smith).

References

Barnhoorn, A., Bystricky, M., Burlini, L., Kunze, K., 2004. The role of recrystallisation on the deformation behaviour of calcite rocks: large strain torsion experiments on Carrara marble. Journal of Structural Geology 26, 885-903.

Beeler, N.M., Tullis, T.E., Blanpied, M.L., Weeks, J.D., 1996. Frictional behavior of large displacement experimental faults. Journal of Geophysical Research 101, 8697-8715.

Beeler, N.M., Tullis, T.E., Goldsby, D.L., 2008. Constitutive relationships and physical basis of fault strength due to flash heating. Journal of Geophysical Research-Solid Earth 113.

Ben-Zion, Y., Sammis, C.G., 2003. Characterization of fault zones. Pure and Applied Geophysics 160, 677-715.

Bestmann, M., Kunze, K., Matthews, A., 2000. Evolution of a calcite marble shear zone complex on Thassos Island, Greece: microstructural and textural fabrics and their kinematic significance. Journal of Structural Geology 22, 1789-1807.

Bestmann, M., Prior, D.J., 2003. Intragranular dynamic recrystallisation in naturally deformed calcite marble: diffusion accommodated grain boundary sliding as a result of subgrain rotation recrystallisation. Journal of Structural Geology 25, 1597-1613.

Boullier, A.M., Yeh, E.-C., Boutareaud, S., Song, S.-R., Tsai, C.-H., 2009. Microscale anatomy of the 1999 Chi-Chi earthquake fault zone. Geochemistry Geophysics Geosystems 10, Q03016, doi:03010.01029/02008GC002252.

Brantut, N., Han, R., Shimamoto, T., Findling, N., Schubnel, A., 2011. Fast slip with inhibited temperature rise due to mineral dehydration: Evidence from experiments on gypsum. Geology 39, 59-62.

Bruhn, R.L., Parry, W.T., Yonkee, W.A., Thompson, T., 1994. Fracturing and Hydrothermal Alteration in Normal-Fault Zones. Pure and Applied Geophysics 142, 609-644.

Burkhard, M., 1990. Ductile deformation mechanisms in micritic limestones naturally deformed at low-temperatures (150-350°C), in: Knipe, R.J., Rutter, E.H. (Eds.), Deformation Mechanisms, Rheology and Tectonics. Geological Society of London, pp. 241-257.

Caine, J.S., Evans, J.P., Forster, C.B., 1996. Fault zone architecture and permeability structure. Geology 24, 1025-1028.

Candela, T., Renard, F., Bouchon, M., Brouste, A., Marsan, D., Schmittbuhl, J., Voisin, C., 2009. Characterization of Fault Roughness at Various Scales: Implications of Three-Dimensional High Resolution Topography Measurements. Pure and Applied Geophysics 166, 1817-1851.

Chester, Logan, J.M., 1987. Composite planar fabric of gouge from the Punchbowl fault, California. Journal of Structural Geology 9, 621-634.

Chester, F.M., Chester, J.S., 1998. Ultracataclasite structure and friction processes of the Punchbowl fault, San Andreas system, California. Tectonophysics 295, 199-221.

Chester, F.M., Chester, J.S., Kirschner, D.L., Schulz, S.E., Evans, J.P., 2004. Structure of large-displacement, strike-slip fault zones in the brittle continental crust, in: Karner, G.D., Taylor, B., Driscoll, N.W., Kohlstedt, D.L. (Eds.), Rheology and deformation in the lithosphere at Continental Margins. Columbia University Press, New York.

Chiarabba, C., Amato, A., Anselmi, M., Baccheschi, P., Bianchi, I., Cattaneo, M., Cecere, G., Chiaraluce, L., Ciaccio, M.G., De Gori, P., De Luca, G., Di Bona, M., Di Stefano, R., Faenza, L., Govoni, A., Improta, L., Lucente, F.P., Marchetti, A., Margheriti, L., Mele, F., Michelini, A., Monachesi, A., Moretti, M., Pastori, M., Piana Agostinetti, N., Piccinini, D., Roselli, R., Seccia, D., Valoroso, L., 2009. The 2009 L'Aquila (central Italy) M_W6.3 earthquake: Main shock and aftershocks. Geophysical Research Letters 36, L18308, doi:18310.11029/12009GL039627.

Chiaraluce, L., 2012. Unravelling the complexity of Apenninic extensional fault systems: A review of the 2009 L'Aquila earthquake (Central Apennines, Italy). Journal of Structural Geology 42, 2-18.

Collettini, C., Viti, C., Tesei, T., Mollo, S., 2013. Thermal decomposition along natural carbonate faults during earthquakes. Geology In Press.

De Paola, N., Collettini, C., Faulkner, D.R., Trippetta, F., 2008. Fault zone architecture and deformation processes within evaporitic rocks in the upper crust. Tectonics 27, TC4017.

De Paola, N., Hirose, T., Mitchell, T., Di Toro, G., Viti, C., Shimamoto, T., 2011. Fault lubrication and earthquake propagation in thermally unstable rocks. Geology 39, 35-38.

Di Toro, G., Goldsby, D.L., Tullis, T.E., 2004. Friction falls towards zero in quartz rock as slip velocity approaches seismic rates. Nature 427, 436-439.

Di Toro, G., Han, R., Hirose, T., De Paola, N., Nielsen, S., Mizoguchi, K., Ferri, F., Cocco, M., Shimamoto, T., 2011. Fault lubrication during earthquakes. Nature 471, 494-498.

Di Toro, G., Hirose, T., Nielsen, S., Pennacchioni, G., Shimamoto, T., 2006. Natural and experimental evidence of melt lubrication of faults during earthquakes. Science 311, 647-649.

Di Toro, G., Niemeijer, A., Tripoli, A., Nielsen, S., Di Felice, F., Scarlato, P., Spada, G., Alessandroni, R., Romeo, G., Di Stefano, G., Smith, S., Spagnuolo, E., Mariano, S., 2010. From field geology to earthquake simulation: a new state-of-the-art tool to investigate rock friction during the seismic cycle (SHIVA). Rend Lincei-Sci Fis 21, 95-114.

Ebert, A., Herwegh, M., Pfiffner, A., 2007. Cooling induced strain localization in carbonate mylonites within a large-scale shear zone (Glarus thrust, Switzerland). Journal of Structural Geology 29, 1164-1184.

Engelder, J.T., 1974. Cataclasis and the generation of fault gouge. Geological Society of America Bulletin 85, 1515-1522.

Faulkner, D.R., Jackson, C.A.L., Lunn, R.J., Schlische, R.W., Shipton, Z.K., Wibberley, C.A.J., Withjack, M.O., 2010. A review of recent developments concerning the structure, mechanics and fluid flow properties of fault zones. Journal of Structural Geology 32, 1557-1575.

Ferri, F., Di Toro, G., Hirose, T., Han, R., Noda, H., Shimamoto, T., Quaresimin, M., de Rossi, N., 2011. Low- to high-velocity frictional properties of the clay-rich gouges from the slipping zone of the 1963 Vaiont slide, northern Italy. Journal of Geophysical Research-Solid Earth 116.

Fondriest, M., Smith, S.A.F., Candela, T., Nielsen, S., Mair, K., Di Toro, G., 2013. Mirror-like faults and power dissipation during earthquakes. Geology 41, 1175-1178.

Fondriest, M., Smith, S.A.F., Di Toro, G., Zampieri, D., Mittempergher, S., 2012. Fault zone structure and seismic slip localization in dolostones, an example from the Southern Alps, Italy. Journal of Structural Geology 45, 52-67.

Giger, S.B., Cox, S.F., Tenthorey, E., 2008. Slip localization and fault weakening as a consequence of fault gouge strengthening - Insights from laboratory experiments. Earth and Planetary Science Letters In Press.

Goldsby, D.L., Tullis, T.E., 2011. Flash Heating Leads to Low Frictional Strength of Crustal Rocks at Earthquake Slip Rates. Science 334, 216-218.

Gratier, J.P., Gueydan, F., 2007. Deformation in the presence of fluids and mineral reactions: Effects of fracturing and fluid-rock interaction on seismic cycles, in: Handy, M.R., Hirth, G., Hovius, N. (Eds.), Dahlem Workshop Reports, Tectonic Faults: Agents of change on a dynamic earth. The MIT Press, pp. 319-356.

Griffith, Nielsen, S., Di Toro, G., Smith, S.A.F., 2010. Rough Faults, Distributed Weakening, and Off-Fault Deformation. Journal of Geophysical Research 115, doi:10.1029/2009JB006925.

Han, R., Hirose, T., Shimamoto, T., 2010a. Strong velocity weakening and powder lubrication of simulated carbonate faults at seismic slip rates. Journal of Geophysical Research 115, B03412, doi:03410.01029/02008JB006136.

Han, R., Hirose, T., Shimamoto, T., 2010b. Strong velocity weakening and powder lubrication of simulated carbonate faults at seismic slip rates. Journal of Geophysical Research-Solid Earth 115.

Han, R., Hirose, T., Shimamoto, T., Lee, Y., Ando, J., 2011. Granular nanoparticles lubricate faults during seismic slip. Geology 39, 599-602.

Han, R., Shimamoto, T., Hirose, T., Ree, J.H., Ando, J., 2007. Ultralow friction of carbonate faults caused by thermal decomposition. Science 316, 878-881.

Heesakkers, V., Murphy, S., Reches, Z., 2011. Earthquake Rupture at Focal Depth, Part I: Structure and Rupture of the Pretorius Fault, TauTona Mine, South Africa. Pure and Applied Geophysics 168, 2395-2425.

Herwegh, M., Kunze, K., 2002. The influence of nano-scale second-phase particles on deformation of fine grained calcite mylonites. Journal of Structural Geology 24, 1463-1478.

Ikari, M.J., Marone, C., Saffer, D.M., 2011. On the relation between fault strength and frictional stability. Geology 39, 83-86.

Jackson, J., 1994. Active Tectonics of the Aegean Region. Annual Review of Earth and Planetary Sciences, 239-271.

Kim, J.W., Ree, J.H., Han, R., Shimamoto, T., 2010. Experimental evidence for the simultaneous formation of pseudotachylyte and mylonite in the brittle regime. Geology 38, 1143-1146.

Kitajima, H., Chester, J.S., Chester, F.M., Shimamoto, T., 2010. High-speed friction of disaggregated ultracataclasite in rotary shear: Characterization of frictional heating, mechanical behavior, and microstructure evolution. Journal of Geophysical Research-Solid Earth 115.

Kohli, A.H., Goldsby, D.L., Hirth, G., Tullis, T., 2011. Flash weakening of serpentinite at near-seismic slip rates. Journal of Geophysical Research-Solid Earth 116.

Li, H., Wang, H., Xu, Z., Pei, J., Li, T., Huang, Y., Song, S.-R., Kuo, L.-W., Sun, Z., Chevalier, M.-L., Liu, D., 2012. Characteristics of the fault-related rocks, fault zones and the principal slip zone in the Wenchuan Earthquake Fault Scientific Drilling Project Hole-1 (WFSD-1). Tectonophysics 584, 23-42.

Logan, J.M., Friedman, M., Higgs, N., Dengo, C., Shimamoto, T., 1979. Experimental studies of simulated gouge and their application to studies of natural fault zones, Proceedings of Conference VIII on analysis of actual fault zones in bedrock. U.S. Geological Survey Open-File Report pp. 79-1239.

Mair, K., Marone, C., 1999. Friction of simulated fault gouge for a wide range of velocites and normal stresses. Journal of Geophysical Research 104, 28899-28914.

Marone, C., 1998. Laboratory-derived friction laws and their application to seismic faulting. Annual Review of Earth and Planetary Sciences 26, 643-696.

Marone, C., Raleigh, C.B., Scholz, C.H., 1990. Frictional behaviour and constitutive modeling of simulated fault gouge. Journal of Geophysical Research 95, 7007-7025.

Mitchell, T.M., Smith, S.A.F., Anders, M.H., Di Toro, G., Nielsen, S., Cavallo, A., Beard, A.D., 2014. Catastrophic emplacement of giant landslides aided by thermal decomposition: Heart Mountain, Wyoming. Earth and Planetary Science Letters In Press.

Mizoguchi, K., Hirose, T., Shimamoto, T., Fukuyama, E., 2008. Internal structure and permeability of the Nojima fault, southwest Japan. Journal of Structural Geology 30, 513-524.

Nielsen, S., Di Toro, G., Hirose, T., Shimamoto, T., 2008. Frictional melt and seismic slip. Journal of Geophysical Research-Solid Earth 113.

Niemeijer, A., Di Toro, G., Nielsen, S., Di Felice, F., 2011. Frictional melting of gabbro under extreme experimental conditions of normal stress, acceleration, and sliding velocity. Journal of Geophysical Research-Solid Earth 116.

Niemeijer, A.R., Spiers, C.J., Peach, C.J., 2008. Frictional behaviour of simulated quartz fault gouges under hydrothermal conditions: Results from ultra-high strain rotary shear experiments. Tectonophysics 460, 288-303.

Otsuki, K., Monzawa, N., Nagase, T., 2003. Fluidization and melting of fault gouge during seismic slip: Identification in the Nojima fault zone and implications for focal earthquake mechanisms. Journal of Geophysical Research-Solid Earth 108, 2192, doi:2110.1029/2001JB001711.

Power, W.L., Tullis, T.E., Brown, S.R., Boitnott, G.N., Scholz, C.H., 1987. Roughness of natural fault surfaces. Geophysical Research Letters 14, 29-32.

Power, W.L., Tullis, T.E., Weeks, J.D., 1988. Roughness and wear during brittle faultin. Journal of Geophysical Research 93, 15268-15278.

Proctor, B., Mitchell, T.M., Hirth, G., Goldsby, D., Zorzi, F., Di Toro, G., 2014. Dynamic weakening of serpentinite gouges and bare-surfaces at seismic slip rates. Journal of Geophysical Research-Solid Earth In Review.

Rathbun, A.P., Marone, C., 2010. Effect of strain localization on fictional behaviour of sheared granular materials. Journal of Geophysical Research 115.

Reches, Z., Dewers, T.A., 2005. Gouge formation by dynamic pulverization during earthquake rupture. Earth and Planetary Science Letters 235, 361-374.

Reches, Z., Lockner, D.A., 2010. Fault weakening and earthquake instability by powder lubrication. Nature 467, 452-455.

Ree, J.H., Ando, J.I., Han, R., Shimamoto, T., 2014. Coseismic microstructures of experimental fault zones in Carrara marble. Journal of Structural Geology 66, 75-83.

Rice, J.R., 2006. Heating and weakening of faults during earthquake slip. Journal of Geophysical Research-Solid Earth 111.

Rodriguez-Navarro, C., Ruiz-Agudo, E., Luque, A., Rodriguez-Navarro, A.B., Ortega-Huertas, M., 2009. Thermal decomposition of calcite: Mechanisms of formation and textural evolution of CaO nanocrystals. American Mineralogist 94, 578-593.

Sagy, A., Brodsky, E., 2009. Geometric and rheological asperities in an exposed fault zone. Journal of Geophysical Research 114, B02301, doi:02310.01029/02008JB005701.

Sagy, A., Brodsky, E.E., Axen, G.J., 2007. Evolution of fault-surface roughness with slip. Geology 35, 283-286.

Sammis, C.G., Ben-Zion, Y., 2008. Mechanics of grain-size reduction in fault zones. Journal of Geophysical Research-Solid Earth 113.

Samtani, M., Dollimore, D., Alexander, K.S., 2002. Comparison of dolomite decomposition kinetics with related carbonates and the effect of procedural variables on its kinetic parameters. Thermochim Acta 392, 135-145.

Sawai, M., Shimamoto, T., Togo, T., 2012. Reduction in BET surface area of Nojima fault gouge with seismic slip and its implication for the fracture energy of earthquakes. Journal of Structural Geology 38, 117-138.

Scholz, C.H., 1987. Wear and Gouge Formation in Brittle Faulting. Geology 15, 493-495.

Scholz, C.H., 2002. The Mechanics of Earthquakes and Faulting, 2 ed. Cambridge University Press, Cambridge.

Schulz, S.E., Evans, J.P., 2000. Mesoscopic structure of the Punchbowl Fault, Southern California and the geologic and geophysical structure of active strike-slip faults. Journal of Structural Geology 22, 913-930.

Scruggs, V.J., Tullis, T.E., 1998. Correlation between velocity dependence of friction and strain localization in large displacement experiments on feldspar, muscovite and biotite gouge. Tectonophysics 295, 15-40.

Scuderi, M.M., Niemeijer, A.R., Collettini, C., Marone, C., 2013. Frictional properties and slip stability of active faults within carbonate-evaporite sequences: The role of dolomite and anhydrite. Earth and Planetary Science Letters, http://dx.doi.org/10.1016/j.epsl.2013.1003.1024.

Sibson, R.H., 1977. Fault rocks and fault mechanisms. Journal of the Geological Society, London 133, 191-213.

Sibson, R.H., 1987. Earthquake Rupturing as a Mineralizing Agent in Hydrothermal Systems. Geology 15, 701-704.

Sibson, R.H., 2003. Thickness of the seismic slip zone. Bulletin of the Seismological Society of America 93, 1169-1178.

Smith, S.A.F., Billi, A., Di Toro, G., Spiess, R., 2011. Principal Slip Zones in Limestone: Microstructural Characterization and Implications for the Seismic Cycle (Tre Monti Fault, Central Apennines, Italy). Pure and Applied Geophysics 168, 2365-2393.

Smith, S.A.F., Di Toro, G., Kim, S., Ree, J.H., Nielsen, S., Billi, A., Spiess, R., 2013. Co-seismic recrystallization during shallow earthquake slip. Geology 41, 63-66.

Sone, H., Shimamoto, T., 2009. Frictional resistance of faults during accelerating and decelerating earthquake slip. Nature Geoscience 2, 705-708.

Stewart, R.A., Reimold, W.U., Charlesworth, E.G., Ortlepp, W.D., 2001. The nature of a deformation zone and fault rock related to a recent rockburst at Western Deep Levels Gold Mine, Witwatersrand Basin, South Africa. Tectonophysics 337, 173-190.

Tenthorey, E., Cox, S.F., 2006. Cohesive strengthening of fault zones during the interseismic period: An experimental study. Journal of Geophysical Research-Solid Earth 111, B09202, doi:09210.01029/02005JB004122.

Tisato, N., Di Toro, G., De Rossi, N., Quaresimin, M., Candela, T., 2012. Experimental investigation of flash weakening in limestone. Journal of Structural Geology.

Togo, T., Shimamoto, T., 2012. Energy partition for grain crushing in quartz gouge during subseismic to seismic fault motion: An experimental study. Journal of Structural Geology 38, 139-155.

Trullenque, G., Kunze, K., Heilbronner, R., Stunitz, H., Schmid, S.M., 2006. Microfabrics of calcite ultramylonites as records of coaxial and non-coaxial deformation kinematics: Examples from the Rocher de l'Yret shear zone (Western Alps). Tectonophysics 424, 69-97.

Verberne, B.A., He, C.R., Spiers, C.J., 2010. Frictional Properties of Sedimentary Rocks and Natural Fault Gouge from the Longmen Shan Fault Zone, Sichuan, China. Bulletin of the Seismological Society of America 100, 2767-2790.

Violay, M., Nielsen, S., Spagnuolo, E., Cinti, D., Di Toro, G., Di Stefano, G., 2013. Pore fluid in experimental calcite-bearing faults: Abrupt weakening and geochemical signature of co-seismic processes. Earth and Planetary Science Letters 361, 74-84.

Wibberley, C.A.J., Shimamoto, T., 2003. Internal structure and permeability of major strike-slip fault zones: the Median Tectonic Line in Mie Prefecture, Southwest Japan. Journal of Structural Geology 25, 59-78.

Yao, L., Ma, S.L., Shimamoto, T., Togo, T., 2013a. Structures and high-velocity frictional properties of the Pingxi fault zone in the Longmenshan fault system, Sichuan, China, activated during the 2008 Wenchuan earthquake. Tectonophysics 599, 135-156.

Yao, L., Shimamoto, T., Ma, S.L., Han, R., Mizoguchi, K., 2013b. Rapid postseismic strength recovery of Pingxi fault gouge from the Longmenshan fault system: Experiments and implications for the mechanisms of high-velocity weakening of faults. Journal of Geophysical Research-Solid Earth 118, 4547-4563.